

Design of the first fusion experiment to achieve target energy gain $G > 1$

A. L. Kritcher,^{1,*} A. B. Zylstra,¹ C. R. Weber,¹ O. A. Hurricane,¹ D. A. Callahan,^{1,†} D. S. Clark,¹ L. Divol,¹ D. E. Hinkel,¹ K. Humbird,¹ O. Jones,^{1,‡} J. D. Lindl,¹ S. Maclaren,¹ D. J. Strozzi,¹ C. V. Young,¹ A. Allen,² B. Bachmann,¹ K. L. Baker,¹ T. Braun,¹ G. Brunton,¹ D. T. Casey,¹ T. Chapman,¹ C. Choate,¹ E. Dewald,¹ J.-M. G. Di Nicola,¹ M. J. Edwards,¹ S. Haan,¹ T. Fehrenbach,³ M. Hohenberger,¹ E. Kur,¹ B. Kustowski,¹ C. Kong,² O. L. Landen,¹ D. Larson,¹ B. J. MacGowan,¹ M. Marinak,¹ M. Millot,¹ A. Nikroo,¹ R. Nora,¹ A. Pak,¹ P. K. Patel,^{1,†} J. E. Ralph,¹ M. Ratledge,² M. S. Rubery,¹ D. J. Schlossberg,¹ S. M. Sepke,¹ M. Stadermann,¹ T. I. Suratwala,¹ R. Tommasini,¹ R. Town,¹ B. Woodworth,¹ B. Van Wonterghem,¹ and C. Wild³

¹Lawrence Livermore National Laboratory, P.O. Box 808, Livermore, California 94551-0808, USA

²General Atomics, P.O. Box 85608, San Diego, California 92186-5608, USA

³Diamond Materials GmbH, 79108 Freiburg, Germany



(Received 24 October 2023; accepted 17 January 2024; published 5 February 2024)

In this work we present the design of the first controlled fusion laboratory experiment to reach target gain $G > 1$ N221204 (5 December 2022) [Phys. Rev. Lett. **132**, 065102 (2024)], performed at the National Ignition Facility, where the fusion energy produced (3.15 MJ) exceeded the amount of laser energy required to drive the target (2.05 MJ). Following the demonstration of ignition according to the Lawson criterion N210808, experiments were impacted by nonideal experimental fielding conditions, such as increased (known) target defects that seeded hydrodynamic instabilities or unintentional low-mode asymmetries from nonuniformities in the target or laser delivery, which led to reduced fusion yields less than 1 MJ. This Letter details design changes, including using an extended higher-energy laser pulse to drive a thicker high-density carbon (also known as diamond) capsule, that led to increased fusion energy output compared to N210808 as well as improved robustness for achieving high fusion energies (greater than 1 MJ) in the presence of significant low-mode asymmetries. For this design, the burnup fraction of the deuterium and tritium (DT) fuel was increased (approximately 4% fuel burnup and a target gain of approximately 1.5 compared to approximately 2% fuel burnup and target gain approximately 0.7 for N210808) as a result of increased total (DT plus capsule) areal density at maximum compression compared to N210808. Radiation-hydrodynamic simulations of this design predicted achieving target gain greater than 1 and also the magnitude of increase in fusion energy produced compared to N210808. The plasma conditions and hotspot power balance (fusion power produced vs input power and power losses) using these simulations are presented. Since the drafting of this manuscript, the results of this paper have been replicated and exceeded (N230729) in this design, together with a higher-quality diamond capsule, setting a new record of approximately 3.88 MJ of fusion energy and fusion energy target gain of approximately 1.9.

DOI: [10.1103/PhysRevE.109.025204](https://doi.org/10.1103/PhysRevE.109.025204)

I. INTRODUCTION

Fusion offers the promise of clean limitless energy, fueled by isotopes of hydrogen, that could be the long-term answer to rapidly growing global energy demands, provide energy security in times of unforeseen political tension, and address climate changes from greenhouse gas emission. Generating more fusion energy than required to generate the fusion reactions has been a long-standing goal of all fusion energy approaches and the last remaining milestone for the National Ignition Facility (NIF) [1] to claim fusion ignition [2]. Ignition is a prerequisite for generating net energy gain in the inertial confinement fusion approach [3,4] and requires reaching

extreme conditions (tens of millions of degrees and hundreds of billions of atmospheres) to overcome the electrostatic repulsion of deuterium and tritium (DT) and enable fusion to occur. Energy is released in the form of a helium (α) particle and a more energetic neutron [$D+T \rightarrow n$ (14.1 MeV)+ ^4He (3.5 MeV)] [5]. These conditions are created by imploding DT fuel at extreme velocities to do mechanical work on a central plasma, or hotspot made up of a small fraction of the initial fuel, using a higher-density shock-compressed DT fuel piston [6]. High areal densities of the DT fuel in the hotspot and surrounding fuel piston are required for absorption of energetic α particles (^4He) born in the fusion process to heat the hotspot plasma (self-heating) and for longer confinement times to enable more of the DT to fuse before the hot compressed fuel explodes under its own pressure and cools the plasma. If sufficient self-heating from absorption of the α particles occurs, the hotspot will ignite and create a burn wave that moves through the remaining cooler fuel piston, significantly increasing the energy output.

*kritcher2@llnl.gov

[†]Present address: Focused Energy Inc., 11525-B Stonehollow Drive, Suite 200, Austin TX 78758, USA.

[‡]Deceased.

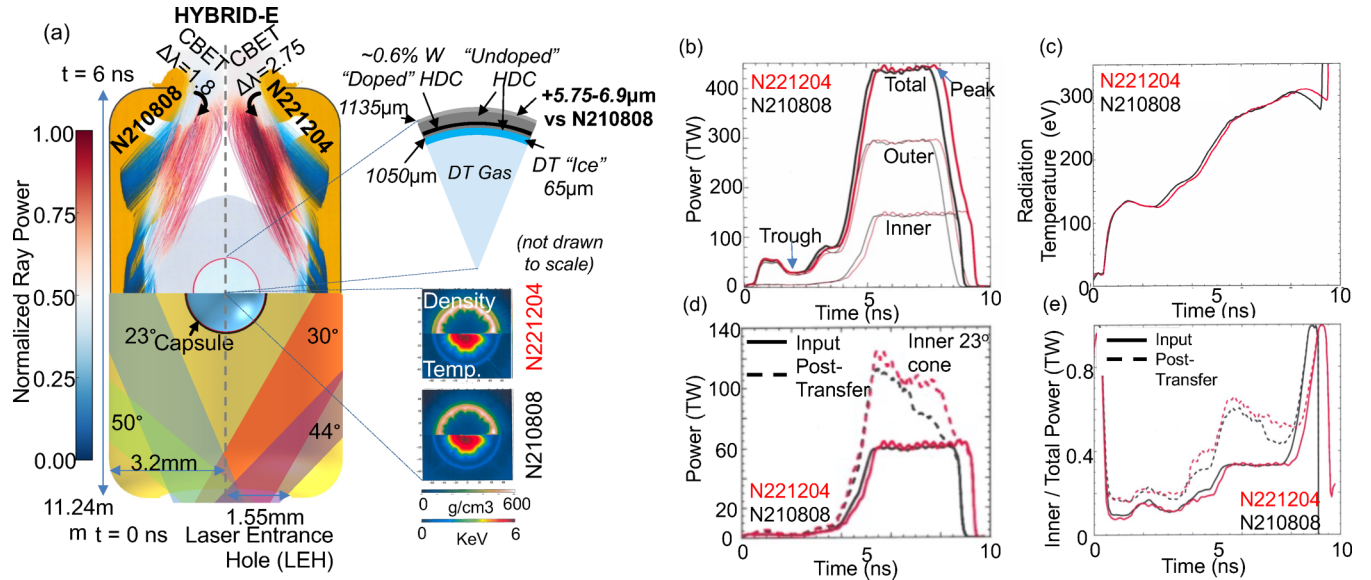


FIG. 1. (a) Schematic of the target configuration showing the hohlraum and spherical diamond capsule that contains DT fuel. Radiation hydrodynamics simulations of the integrated hohlraum and capsule (top) show the material positions and plasma filling into the hohlraum at time equal to 6 ns for N221204 (right) compared to N210808 (left). Also shown are simulated laser ray powers and an expanded view of the density and temperature at stagnation for N221204 vs N210808 from α -off simulations (simulations where α -particle deposition is turned off). (b) The radiation drive symmetry was controlled by transferring energy between laser beams through wavelength detuning $\Delta\lambda$ and by precisely defining the balance of laser powers between the inner (23° and 30°) and outer (44° and 50°) beams throughout the duration of the laser pulse. The peak of the laser power was extended by about 300 ps to drive the thicker diamond capsule and the trough was lengthened to preserve the shock timing. (c) The simulated hohlraum internal radiation temperature T_{rad} as a function of time shows the extended and higher radiation temperature for N221204 compared to N210808. The near vertical rise of T_{rad} at the end of the drive for both cases is due to reheating [17] of the hohlraum from the capsule fusion output. (d) Calculated change in inner cone power (e.g., on the 23° cone) post energy transfer. This amount of transfer was increased for N221204 (red lines) compared to N210808 (black lines) via increasing $\Delta\lambda$ from 1.8 Å to 2.75 Å to maintain symmetry with the longer laser pulse and thicker ablator. (e) Ratio of the full inner cone power to total laser power for the incident laser pulse (solid lines) and post-transfer pulse (dashed lines).

Ignition by the Lawson criterion [7] was first demonstrated at the NIF on 8 August 2021 (NIF shot No. N210808) [8–10] by optimizing the implosion design from the HYBRID-E burning plasma platform [11] and increasing the energy density of the hotspot, as well as the target quality (the diamond capsule that holds the DT fuel). While achieving ignition by the Lawson criterion, N210808 only produced approximately 70% of the laser energy required to drive the experiment as fusion energy. In addition, follow-on experiments showed variability to nonideal experimental fielding conditions that lowered the performance to 30%–50% that of N210808. These perturbations include unintentional low-mode asymmetries and hydrodynamic instabilities seeded by compromised diamond capsule quality that caused mixing of high-Z material into the hotspot plasma.

This work presents the first fusion design to ever produce more fusion energy than energy delivered to the target, or target gain greater than one, in a laboratory setting, and is the current record holder for fusion energy produced at the NIF (3.88 MJ and target gain of approximately 1.5–1.9 \times). Also see the accompanying papers which describe the experimental results [12], ignition criteria and theory [13], and the historical perspective [14]. This design provided more margin for achieving high fusion yields in the presence of perturbations from nonideal experimental conditions that reduced performance in the preceding N210808 design, which still achieved ignition by the Lawson criterion (e.g., large

mode 1 and 2 asymmetries). Intentional design changes were made to increase the areal density of the DT fuel and capsule at maximum compression, which resulted in an increase in performance and fuel burnup fraction.

Prior attempts to increase the DT areal density ρR through higher convergence have been unsuccessful in improving the performance and contradictory to expectations from high-fidelity plasma physics simulations, likely as a result of increased instabilities that accompany this method of increasing the ρR . Here we increase the thickness of the diamond capsule that holds the DT fuel to increase the total (DT plus capsule) areal density, which is enabled by increasing the laser driver energy on target and adjustments to the implosion symmetry. These changes were proposed directly following N210808, outlined in [9], enabled by improvements to the laser driver efficiency [15,16].

II. EXPERIMENTAL DESIGN

Figure 1(a) shows a schematic of the target and laser configuration. This design uses the indirect-drive approach [18–20], where laser beams are pointed onto the inside of a gold-lined depleted uranium cylindrical can (hohlraum), 11.24 mm length \times 6.4 mm diameter, in four distinct laser sets defined by their angle of incidence (inner beams 23° and 30° and outer beams 44° and 50°). This creates a near blackbody radiation oven that is approximately 3×10^6 K (greater than

300 eV) [see Fig. 1(c)]. The x rays are absorbed in the outside region of a hollow diamond spherical capsule (ablator) (1050- μm inner radius and approximately 85 μm thick) sitting in the center of the hohlraum, which contains the DT fuel (65- μm -thick ice layer with a DT gas core). The x-ray absorption heats and ablates the diamond, which expands radially outward, causing the remaining diamond capsule and DT fuel to be accelerated inward, or imploded, via the rocket effect at extreme implosion velocities ($v_{\text{imp}} \sim 380\text{--}400$ km/s).

A key change in the target configuration for the N221204 design was to thicken the diamond capsule holding the DT fuel by approximately 5.75 μm (N221204) and 6.9 μm (N230729) compared to N210808 to provide higher-energy coupling of the radiation drive to the hotspot, higher total areal density at peak compression, and improved stability. The amount of percent W dopant in the diamond was also increased compared to N210808 (see the Appendix). The increase in areal density at maximum compression for the N221204 design vs N210808 can be seen in Fig. 1(a) (expanded view), showing the increase in density of the DT shell (top) surrounding the DT hotspot (bottom) from radiation hydrodynamics simulations with the impact of α heating turned off (α off).

The laser energy was increased from 1.92 to 2.05 MJ at constant peak laser power (approximately 440 TW) by extending the peak of the pulse by 300 ps [see Fig. 1(b)]. The trough of the laser pulse was also extended by 150 ps to maintain the shock timing for the thicker capsule. This resulted in higher and longer duration radiation temperatures compared to N210808 [see Fig. 1(c)]. These first experiments were required to increase energy at constant laser power (vs increasing the laser power) as part of the risk mitigation for optics damage in the first stage of enhancing the laser capability. In this work, thicker ablators were used to make optimal use of the extra drive at the end of the pulse, which would have otherwise not coupled significantly more driver energy to the implosion. Work is ongoing to further increase the laser power and energy (480 TW and 2.2 MJ), which will be used to drive even thicker (approximately 10–16 μm) diamond capsules to high implosion velocities approximately 400 km/s and low coasting time [21], the time between when the radiation drive cools and peak compression.

The longer laser pulse results in more plasma filling into the hohlraum, making it difficult for the inner laser beams to propagate to the hohlraum center, creating a reduction in x-ray drive, a more oblate implosion, and reduced energy coupling to the hotspot [22]. The uniformity of the radiation drive was controlled by increasing the amount of laser energy transfer from the outer to the inner beams, or cross-beam energy transfer (CBET), by increasing the detuning of their relative wavelengths [$\Delta\lambda = (\text{inner beam}) - (\text{outer beam})$ before laser frequency tripling] [23–26], where $\Delta\lambda = 1.8$ \AA for N210808 and $\Delta\lambda = 2.75$ \AA for N221204. An important advancement for controlling symmetry was the development [25] of CBET in hohlraums with low amounts of He gas fill (0.3 mg/cm³) [27–29] which achieved high levels of laser light coupling to the hohlraum, approximately 96%–99%, and low amounts of backscattered laser light. See the Appendix for a detailed accounting of the laser energy balance into the hohlraum and the implosion.

Figure 1(a), top, shows radiation hydrodynamics simulations of N221204 (right) compared to N210808 (left) at 6 ns after the start of the laser pulse, with the calculated positions of the material boundaries [gold-lined depleted uranium hohlraum (orange), high-density carbon (HDC) ablator (light gray), and DT ice layer (blue)]. Overlaid are simulated laser rays showing propagation and absorption within the hohlraum, where the color corresponds to normalized laser powers after CBET. Since the amount of late-time drive symmetry can be difficult to accurately model, a semianalytical model [30] and measured sensitivity curves [9] were used to determine the optimal $\Delta\lambda$. In addition, precisely adjusting the specific powers on the inner and outer laser cones during the entire laser pulse [Fig. 1(b)] enabled controlling fluctuations in the radiation drive uniformity, which can induce ρR variations in the compressed fuel and reduce energy coupling. Detailed radiation hydrodynamic simulations using HYDRA [31] with inline CBET [32] were used to design the specific inner and outer powers. Figure 1(d) shows the calculated increase in power following CBET (e.g., on the 23° cone) and Fig. 1(e) shows the calculated increase in total inner cone power to total power post CBET together with the input request (see also the Appendix).

These design changes were predicted to increase a key ignition metric EP^2 (by approximately 25% compared to N210808), using radiation hydrodynamic simulations, where E is the hotspot internal energy and P is the hotspot pressure at bang time from α -off simulations [33] [see Fig. 2(a), red shaded region, for this work]. Increasing the ignition margin enables igniting the hotspot plasma in the presence of unintentional perturbations, e.g., low-mode asymmetries [22,34–37] and radiative loss from ablator mixing into the hotspot [38], and improved robustness for achieving greater than 1-MJ yields. This increase is also expected from analytical theory, which predicts EP^2 to increase as the cube of the increased shell mass, assuming symmetry and other implosion parameters could be held constant, giving a 23% increase in EP^2 for an 8% increase in shell mass [13,39]. The colored points are inferred quantities from prior experiments where the impact of α heating is removed to better assess proximity to the ignition boundary (black dashed curves) [40]. The gray points under the ignition boundary are from simulations and the red shaded region for this design includes various simulation models to assess the expected increase in EP^2 . Experiments to the right of the ignition boundary result in higher burnup of the DT fuel as the burn-wave postignition moves into the cooler denser DT shell. Figure 2(b) shows the tradeoffs in various [one-dimensional (1D)] implosion metrics that were considered when designing the precise increase in diamond ablator thickness compared to N210808. Following ignition of the hotspot, the simulated fusion energy produced (neutron yield α , black curve) increases with increasing total areal density of the fuel and ablator at peak compression (ρR , magenta curve), which provides increased self-heating, hotspot confinement, and burnup fraction of the DT fuel [41]. Higher total areal densities can be achieved by driving thicker, higher-mass HDC capsules. However, there is a limit on the amount of fuel and capsule mass that can be experimentally driven and still ignite with a fixed driver energy capability and in the presence of non-1D perturbations. These (1D)

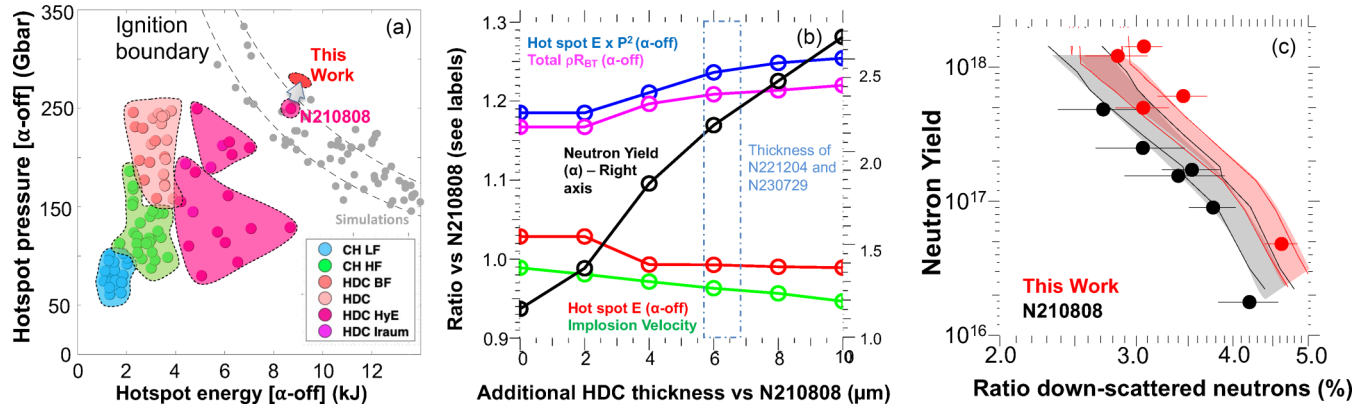


FIG. 2. (a) Increase in ignition metric EP^2 : inferred hotspot pressure P and internal energy E for previous DT layered experiments at NIF in relation to the ignition boundary (black dashed lines denote approximately EP^2). The gray points under the ignition boundary are from simulations. The increase in ignition metric EP^2 for the N221204 design compared to N210808 is shown in the red shaded region, calculated using a range of assumed perturbations (1D and 3D effects). (b) Tradeoffs in implosion metrics with increased capsule thickness: ratio of simulated 1D implosion metrics compared to N210808 as a function of increased HDC ablator thickness. The calculated hotspot E , hotspot EP^2 , and total areal density ρR are taken at peak compression or bang time (peak neutron production) from simulations with α off. The calculated peak implosion velocities and fusion neutron yields are also shown. (c) Increase in areal density for this work compared to N210808: neutron yield as a function of DSR, ratio of downscattered neutrons to primary neutrons. Black and red circles are data and the shaded curves are simulations showing the expected increase in DSR at a given yield for this new design from 1D simulations and considering potential 3D degradations (see the text for details).

simulations reach higher yields than the experiments and approach the theoretical fuel burnup fraction. Two-dimensional calculations which reproduce the N210808 experimental yield (see Table I) predict a larger relative increase in performance for the thicker-ablator design.

At constant peak laser power, an approximately 5.75–6.9- μm -thicker diamond ablator enabled coupling more of the extended radiation drive to the implosion (approximately +20 kJ vs N210808) vs extending the drive at constant thickness (approximately +3 kJ vs N210808). This enabled reaching similar hotspot internal energies (red curve) compared to N210808, even with the reduced fuel implosion velocity (green curve) from the extra target mass at constant laser power. Here additional PdV work is being done on the hotspot by the imploding remaining ablator material.

One of the goals of this design was to increase the margin for ignition (approximately EP^2) in the presence of known perturbations that reduce the hotspot internal energy or pressure. In choosing a starting thickness, we consider that the hotspot internal energy eventually declines as thickness is increased and the velocity is reduced from the extra mass of the ablator. There exists a theoretical minimum velocity required to ignite the hotspot for a given total areal density [41] which can be degraded by known issues, low modes, and ablator mixing into the hotspot. In addition, thicker ablators are generally more challenging for symmetry due to the longer laser pulse required to maintain shock timing. Therefore, the target thickness increase of approximately 5.75–6.9 μm was initially chosen to increase ρR while considering the reduction in implosion velocity and maintaining E . The coast time was also considered as lower implosion velocity leads to later bang times for the same radiation drive and thus longer coast times.

Future plans will increase the thickness of the ablator by another 4–10 μm to explore the tradeoff in ignition margin

vs fuel burnup fraction. Two-dimensional total degradation calculations of these designs give greater than $3\times$ higher yield compared to this work if symmetry can be maintained and ignition can still be achieved. We also see an increased robustness for the thicker-ablator design, or less sensitivity of neutron yield to various degradation mechanisms compared to the present work.

Previously, attempts to increase ρR via higher-convergence lower-adiabat implosions did not result in higher performance due to enhanced instabilities [42]. As intended, this design increased performance and yielded amplification as a result of design changes that increased ρR . The increase in ρR can be observed experimentally by looking at the downscattered ratio (DSR) of primary neutrons in the dense DT surrounding the hotspot with the relationship $\text{DSR} \sim (\rho R_{\text{DT}} + \rho R_{\text{HDC}}/8)/19$ [33]. Figure 2(c) shows the simulated expected increase in DSR at a given neutron yield for the N221204 design (red shaded region) compared to the N210808 (black shaded region). Following maximum compression, ρR is reduced as the implosion expands and is expected to be lower as yield is increased for a given design. Therefore, it is important to compare ρR improvements at similar fusion yields (see Fig. 7 in the Appendix).

Since the DSR is weighted more toward the fuel ρR vs the total (fuel plus ablator) ρR , the expected increase in DSR at the observed yield level was 7% (see Fig. 7 of the Appendix for the simulated fuel, ablator, and total ρR). However, the total (DT plus capsule) ρR is a better metric for improved yield amplification than just the fuel ρR , which was calculated to be a larger increase relative to N210808 for this design, approximately 20% α off and approximately 15% at higher yields. The shaded region spans the 1D calculated DSR to possible 3D effects, and the closed black circles are experimental data from N210808 and the variability experiments. Achieving a higher DSR at a given yield indicates improvement in the

TABLE I. Simulation metrics for N221204 compared to N210808 and measurements. Here DSR is defined as the ratio of the escaping 10–12-MeV neutrons to the 13–15-MeV neutrons. The subscript BT is taken at the time of maximum neutron production and α -off metrics correspond to calculations where the α heating is artificially turned off. Data are listed in parentheses and simulations are listed on the upper cell lines.

Total degradation simulation ^a [less asymmetry, ^b without low modes ^c] (Data)	N210808	N221204
fusion yield E_F (MJ)	1.26 [2.25,7.6] (1.37 \pm 0.04)	3.0 [7.2,13.6] (3.15 \pm 0.16)
bang time (ns)	9.27 [9.28,9.27] (9.28 \pm 0.07)	9.61 [9.61,9.58] (9.53 \pm 0.07)
DT ion temperature (keV)	10.4 [11.6,20] (10.86 \pm 0.37)	13.13 [19,27] (13.07 \pm 0.74)
adiabat	2.55–2.75	2.22–2.68
DSR (%)	3.17 [3.0,2.73] (2.72 \pm 0.24)	2.93 [2.85,3.08] (2.68 \pm 0.16)
burn width (ps)	69 [61,39] (89 \pm 15)	63 [37,33] (70 \pm 25)
implosion velocity (km/s)	401	383
remaining ablator mass (%)	3.8	5.7
total ρR_{BT} α off (g/cm ²)	1.35 [1.38, 1.5]	1.41 [1.5, 1.7]
total ρR_{BT} (g/cm ²)	1.04 [0.94, 0.87]	0.97 [0.95, 1.12]
HDC ρR_{BT} (g/cm ²)	0.34 [0.31, 0.28]	0.38 [0.35, 0.4]
fuel ρR_{BT} (g/cm ²)	0.67 [0.60, 0.57]	0.55 [0.55, 0.68]
hotspot ρR_{BT} (g/cm ²)	0.44 [0.54, 0.56]	0.56 [0.56, 0.65]
hotspot pressure P_{BT} (Gbar)	503 [577, 1070]	657 [1315, 1969]
hotspot internal energy E_{BT} (kJ)	85 [147, 374]	181 [332, 533]
yield amplification ^d	29 [50,133]	70 [160,290]
$G_{\text{target}} (E_F/E_{\text{laser}})$	0.65 [1.2,4] (0.71)	1.5 [3.5,6.6] (1.54)

^aTotal degradation high-resolution 2D capsule simulations with material roughnesses, a model for the tent and fill tube perturbations, and low-mode asymmetries from the hohlraum (Legendre modes P1, P2, and P4).

^bTotal degradation^a 2D simulations with reduced level of P2 flux asymmetry during the peak of the drive by 75%.

^cTotal degradation^a 2D simulations without the low-mode asymmetries from the hohlraum.

^dRatio of the yield in simulations where α particles deposit energy in the hotspot (burn on) vs stream freely out of the problem (burn off; no α).

design areal density, which was observed experimentally [12] (black and red points) and by more than the expected amount for the N221204 design compared to the N210808 design [12], and ultimately led to higher burnup fractions of the DT fuel for N221204 (approximately 4%) compared to N210808 (approximately 2%). The experimental DSR of N221204 repeat experiments including N230729, the highest-gain experiment to date which used a higher-quality diamond capsule compared to N221204, are also shown and give the highest measured compression vs yield curve for diamond to date.

Thicker ablators are also better for hydrodynamic stability at the interface between the DT fuel and the diamond ablator, which showed a significant reduction in calculated Atwood number for this design compared to N210808 (see Fig. 8 of the Appendix). This is important for maintaining a higher “clean” (unmixed) fraction of DT ice as mixing of ablator material into the ice layer can impact compressibility, result in bremsstrahlung losses, and reduce fuel heating. This reduction of ablator mixing into the ice was observed experimentally for this design, confirming the improvement in stability [12].

III. INCREASED-YIELD MARGIN

Figure 3 shows the calculated increase in performance margin (shown in units of neutron yield where 1×10^{18} neutrons are approximately equal to 2.8 MJ of total fusion energy produced) for the N221204 design in this work (red circles and curves) compared to the N210808 design (black circles and curves) as unintentional perturbations that can reduce the fusion yield are increased. Here the perturbation magnitude is artificially increased in simulations with larger values along the x axes. The higher-yield margin of the N221204 design enables producing both more than 1 MJ of fusion energy in the presence of enhanced perturbations compared to N210808 and higher yields if the same low level of perturbations as observed on N210808 can be achieved. The types of perturbations shown in Fig. 3 are main sources of yield degradation in nearly all of the ignition experiments and are difficult to control; therefore, increasing the margin to these perturbations is important.

Figure 3(a) shows higher 2D simulated neutron yield for N221204 vs N210808 as a function of increased surface

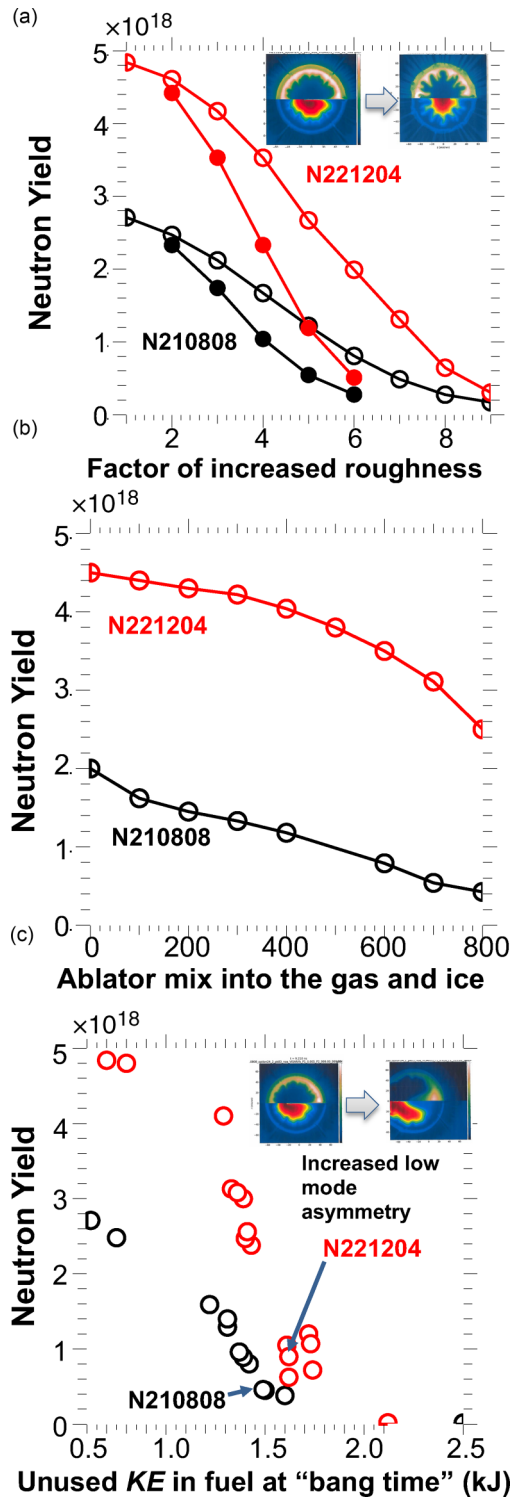


FIG. 3. Simulated performance for the N221204 design (red curve and circles) compared to the N210808 design (black curve and circles) for a range of values of various perturbations including instabilities from (a) ablator and ice roughness (open circles vary ablator roughness with fixed $1\times$ roughness on the ice and closed circles vary the ice and ablator roughness), (b) ablator mixing into the hotspot, and (c) low-mode asymmetries from the radiation drive (see the text for details).

roughness (as factors of the nominal values) on the tungsten-doped and -undoped diamond ablator interfaces and $1.0\times$ roughness on the ice (open symbols) as well as roughness applied to the doped and undoped interfaces as well as the ice layer as denoted by the x axis (closed symbols). These simulations model the tent perturbation feature, DT fill-tube perturbation feature, and surface roughnesses (total degradation 2D simulations without the low-mode asymmetries from the hohlraum in Table I). This perturbation can arise from worse target and ice-layer quality and also act as a surrogate in simulations for increased interface instability. Example simulated images from α -off simulations are shown as insets for the nominal case and an increased roughness case. The top half of the inset shows the density contour at peak compression and the bottom half shows the ion temperature at peak compression.

Figure 3(b) shows higher neutron yield for the N221204 design vs the N210808 design to a given level of ablator mixing into the inner $10\ \mu\text{m}$ of DT ice and volumetrically into the hotspot (mass in nanograms), which can radiate energy away and cools the hotspot. Here the calculations use nonlocal thermodynamic equilibrium atomic physics tables in one dimension to accurately model the radiative losses. This mixing can be seeded by isolated defects in the diamond ablator such as pits on the outer diamond surface, voids in the diamond shell, engineering features, and hohlraum material that can flake onto the capsule. In this design, increasing the amount of energy coupled to the hotspot enables tolerating higher levels of these isolated capsule defects.

Higher simulated performance for the N221204 vs N210808 design as a function of increased low-mode asymmetries is shown in Fig. 3(c), using total degradation 2D simulations (see Table I) with varying amounts of applied modes P1, P2, and P4, Legendre moments of the radiation flux asymmetry. Here the x axis is the amount of leftover work that was not done on the hotspot, or residual kinetic energy from α -off simulations, as a result of the low-mode asymmetries creating an inefficient piston. As a result, the N221204 design can tolerate higher levels of this perturbation and still achieve high performance compared to N210808. These low-mode asymmetries are another leading source of degradation for ignition experiments, which can be seeded by nonuniformities in the capsule and ice thicknesses as well as imbalances in the laser power delivery. Simulations estimate that the low-mode asymmetries still resulted in a $4.5\times$ yield reduction for N221204, compared to a 32% yield reduction from roughness on the diamond and ice interfaces. Work is ongoing to improve these asymmetries for higher performance.

In addition to improving these perturbations, ongoing work aims to further increase the performance margin and robustness, or insensitivity, to these perturbations. This can be seen in Fig. 4, which shows that the yield can be substantially increased for a given level of increased roughness of the ablator and ice interfaces by further increasing the diamond thickness of the N221204 design using the same hohlraum configuration, laser energy, and adjusted shock timing. These changes are expected to increase total areal density and energy coupled to the implosion. The tradeoff of this design change is

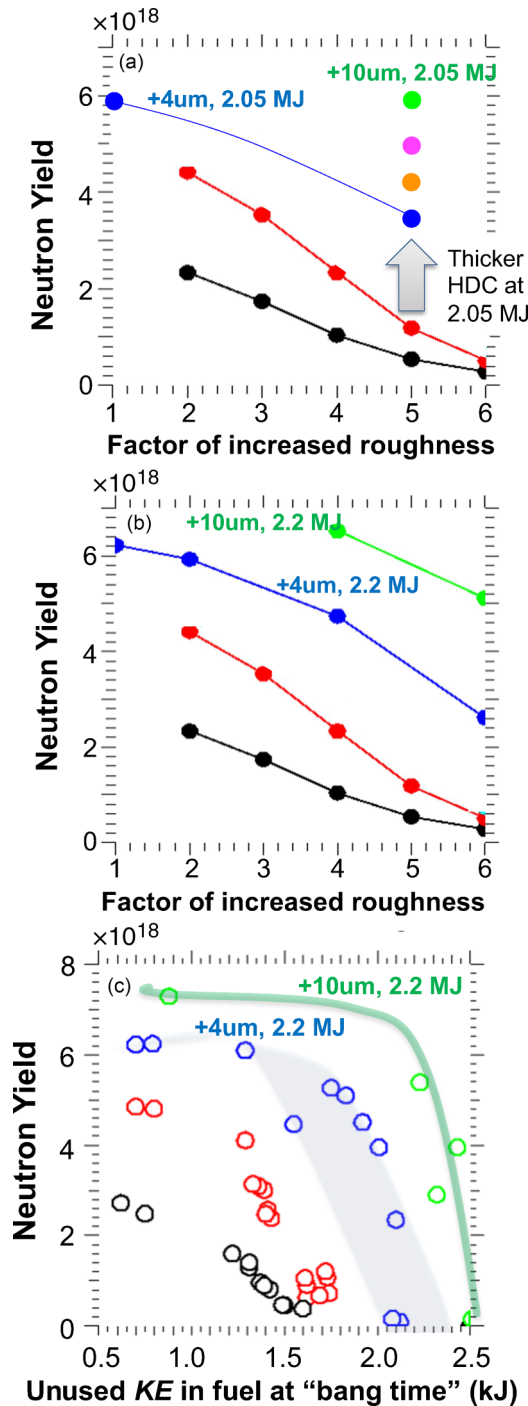


FIG. 4. (a) Simulated yield as a function of roughness of the diamond ablator interfaces and ice layer for future designs that increase the diamond ablator thickness compared to N221204 (red curve) by an additional 4 μm (blue circles), 6 μm (orange circles), 8 μm (magenta circles), and 10 μm (green circles) using the same 2.05 MJ laser energy and hohlraum geometry with adjusted shock timing. (b) Simulated performance as a function of roughness of the diamond and ice layers and (c) increased low-mode asymmetries from the radiation drive for designs that increase the diamond ablator thickness compared to N221204 (red curve) by an additional 4 μm (blue circles) and 10 μm (green circles) using 2.2 MJ of laser energy and hohlraum geometry with adjusted shock timing. The black circles and curves are simulations of the N210808 design.

reduced velocity due to the extra ablator payload and risk for achieving symmetry due to the longer pulse (adjusted shock timing) and extra ablator payload.

The first tests of the thicker-ablator higher-energy design (this work) managed these risks by taking a substantial but smaller first step. Future experiments will continue to pursue thicker ablators using 2.05 MJ of laser energy. In addition, the robustness and yield margin can be further increased with the thicker ablators using an extended 2.2-MJ laser driver [see Fig. 4(b) for the yield vs roughness factor and Fig. 4(c) for the yield vs low-mode asymmetry]. For the 2.2-MJ design with a 10- μm -thicker diamond ablator compared to N221204 (green curves) the yield vs perturbation becomes less sensitive, i.e., more robust. We predict that these designs meet the threshold for minimum velocity to ignite the hotspot and would further increase the total areal density for higher fuel burnup fraction. Additional design modifications are predicted to improve performance by more than $2\times$ and will be tested sequentially, including increasing the laser power of the 2.05- and 2.2-MJ designs up to 500 TW to increase the coupling and implosion velocity, reducing the central gas fill in the capsule for higher convergence, and increasing the DT fuel mass.

The extra margin in performance of the N221204 design, compared to N210808, to low-mode asymmetries was demonstrated on the first test of the new thicker-ablator higher-energy design on 19 September 2022 (N220919), which had a significant level of P2 asymmetry in the hotspot plasma ($P2 \sim -12 \mu\text{m}$), reducing energy coupling to the hotspot. However, due to the increase in performance margin, this experiment still produced a high fusion energy of approximately 1.22 MJ and was the second experiment on NIF to reach greater than 1 MJ. We estimate that this level of asymmetry would have reduced the yield to less than 1×10^{17} neutrons (less than 280 kJ) in the N210808 design. Changes made to improve only this asymmetry between N220919 and N221204 resulted in a greater than $2.5\times$ increase in fusion energy yield (3.15 MJ) and the first controlled fusion experiment to ever reach target gain greater than unity (approximately 1.5). The symmetry changes include increasing the amount of wavelength separation from $\Delta\lambda = 2.5 \text{ \AA}$ to $\Delta\lambda = 2.75 \text{ \AA}$ and optimizing the time-dependent radiation drive symmetry based on an updated model tuned to data which was acquired in 2022 (see the Appendix for more details).

The expected increase in yield as a result of fixing the symmetry was accurately predicted using a HYDRA total degradation model calibrated to N220919 (see Fig. 5). Here the red circles are simulations of the dependence of the neutron yield on the level of hotspot oblateness (P2) for the N221204 thicker-ablator higher-energy design. The level of oblateness is calculated by taking the Legendre decomposition of the 17% peak neutron or x-ray-emission contour. The range of simulated neutron yields at a given level of hotspot oblateness is due to uncertainty in the calculated time history of fluctuations in hotspot and dense DT fuel asymmetry. The insets are simulated contours at peak compression from α -off simulations of the the hotspot temperature (left) and dense DT fuel shape (right) for example points. The measured level of hotspot oblateness for N220919 vs N221204 (blue circles) follows the simulation curve, which predicted that fixing the symmetry would result in target gain

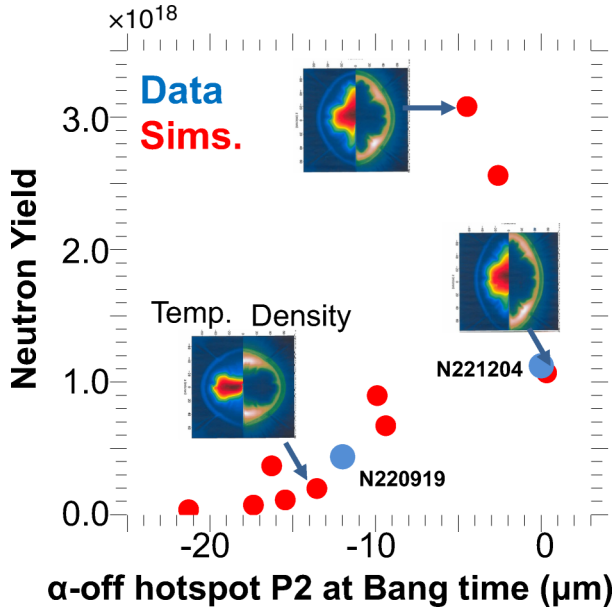


FIG. 5. Simulated sensitivity of α -on fusion energy yield to hotspot oblateness (P2) from α -off simulations, using a total degradation model of the N221204 design (red circles), where the flux asymmetry was adjusted in the simulations to vary hotspot P2. The hotspot P2 was approximately $-12 \mu\text{m}$ for N220919 and approximately $0 \mu\text{m}$ for N221204. We predicted that a performance increase of greater than $2\times$ vs N220919 could be achieved by improving the hotspot P2 to within a few microns of round and a higher increase in performance if the hotspot was closer to round ($P2 = 0$). The range of yields at a given level of hotspot P2 results from different assumptions about the magnitude of the time-varying P2 of the hotspot and DT shell, which will be benchmarked against data in coming experiments.

greater than unity and achievement of ignition at the NIF by all metrics including the National Academy of Sciences definition.

A mode 1 asymmetry also varied between these experiments, with a measured hotspot velocity of 36 km/s for N221204 compared to 67 km/s for N210808. Since the sensitivity of neutron yield to mode 1 asymmetry is design dependent and depends on the presence of other sources of yield degradation, it is important to estimate the impact of mode 1 in simulations that include the other known sources of degradations (P2, P4 tent, fill tube, and roughness) and also match the experimental neutron yield.

From simulations we estimate that the measured mode 1 reduced the yield by approximately 25% for N210808 and by less than 10% for N221204 and that the difference in neutron yield between these experiments as a result of mode 1 was approximately 10%. However, the neutron yield increased by more than $2.5\times$ with the P2 asymmetry correction, which was the dominant source of improved symmetry. In addition, a repeat experiment of N221204 (N230729) displayed a higher observed mode 1 asymmetry of approximately 104 km/s (also simulated to reduce the neutron yield by approximately 25%) but still achieved the highest yield to date of 3.88 MJ and greater than $2.8\times$ higher neutron yield than N210808. The experimental sources for the observed mode 1 asymmetries in these experiments will be outlined in elsewhere.

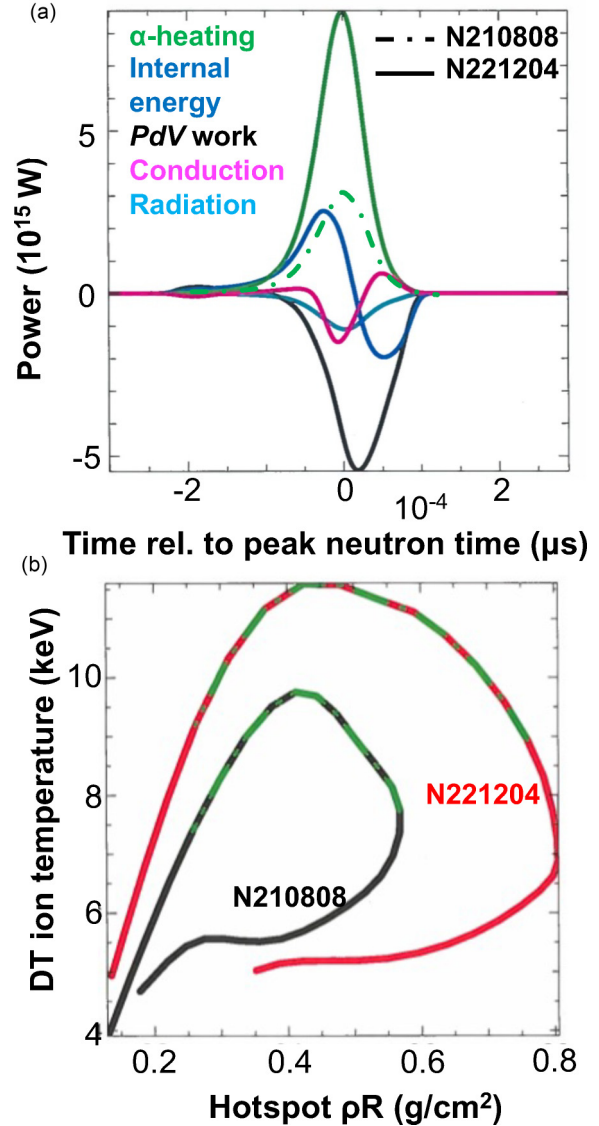


FIG. 6. (a) Temporal histories of the simulated hotspot power (in watts) balance for N221204 (dashed curves) compared to N210808 (solid curves), normalized to the respective bang times (peak neutron production) showing significantly higher α heating for N221204. (b) Simulated hotspot areal density vs ion temperature for N221204 (red curve) vs N210808 (black curve) showing higher initial areal densities for N221204 and a substantial increase in areal density and ion temperature over the burn duration. Here a bang time of $\pm 50 \text{ ps}$ is denoted by the green dashed curves.

We also used a cognitive-simulation machine learning model to generate a probability distribution for achieving target gain greater than unity given these design parameters and previously observed levels of degradations, which predicted a 50% chance for this new design to achieve target gain greater than unity compared to 17% for N210808 [43].

IV. SIMULATED HOTSPOT CONDITIONS

Figure 6 shows these design changes resulted in a substantial increase in calculated α heating power (in watts) for N221204 (solid lines) compared to N210808 (dashed line).

The amount of simulated self-heating power from the α particles is approximately $3\times$ higher for N221204, which burned up approximately $2.3\times$ more DT fuel. The difference in simulated increase in the α heating power compared to the burnup fraction for these experiments is due to differences in the burn duration and in the magnitude of the power loss mechanisms.

This analysis uses detailed radiation hydrodynamic (HYDRA) post-shot total degradation simulations that match the experimental hotspot observables (see Table I). Here the time axis is shifted relative to the time of peak neutron production. The α -particle heating for N221204 (green curve) is greater than the initial PdV work done on the hotspot (black curve) as well as the energy loss mechanisms (conduction and radiative loss), and for a long enough duration of time (confinement time), which enables the plasma to ignite, and a thermodynamic instability in DT plasma, self-heating occurs. The α heating power is so high that the internal energy (blue curves) continues to rise even in the presence of losses, including energy loss resulting from the explosion phase when the PdV work becomes negative and removes energy from the hotspot.

The increase in calculated α heating power is largely due to the increase in calculated hotspot areal density for N221204 vs N210808. This increase can be seen in Fig. 6(b), which shows the evolution in time of the hotspot ρR vs ion temperature for N221204 (red curve) vs N210808 (black curve). The overlaid green dashed curves denotes a bang time of ± 50 ps. Here N221204 starts out at a similar hotspot temperature but higher hotspot areal density, which leads to an increase in α heating and then a substantial increase in hotspot ρR and temperature. The reversal of the trajectory to lower areal densities throughout the burn for both experiments is due to the hotspot continuing to increase in temperature on expansion.

V. CONCLUSION

In summary, the design changes presented in this paper resulted in the first ever controlled fusion experiment (N221204) to exceed target gain greater than unity, where the fusion energy produced exceeded the energy used to drive the target by approximately $1.9\times$. This design used a thicker diamond capsule (additional approximately 7.6% in thickness) together with an extended higher-energy laser drive (additional approximately 7% in energy) [15,16] to increase the margin for ignition and enable higher DT fuel burnup fractions compared to N210808 (approximately 4.3% compared to approximately 1.9%). This proof-of-principle experiment demonstrates that there is nothing fundamentally limiting fusion energy gain in the laboratory. Since this manuscript was drafted, a repeat experiment with a higher-quality diamond ablator (fewer high-Z inclusions) resulted in a new record yield of approximately 3.88 MJ and fusion energy target gain of approximately 1.9. Small adjustments to the laser input conditions were also made for the new capsule.

This work builds on the previous HYBRID-E design N210808 and further increases the α -off total areal density by approximately 20%, which led to a DSR increase at a given yield of greater than 14%, which was higher than predicted. The first test of this new design (N220919) showed an intrinsic P2 asymmetry from the hohlraum radiation drive but still produced a fusion energy of approximately 1.2 MJ. Changes

only to optimize the implosion symmetry for N221204 resulted in a greater than $2.5\times$ increase in fusion energy as predicted by high-fidelity radiation hydrodynamic simulations and theoretical models. This platform will be the basis for future designs, including an effort to extend the laser drive to 2.2 MJ and increase the HDC ablator thickness by an additional approximately 10 μm .

ACKNOWLEDGMENTS

This work was performed under the auspices of U.S. Department of Energy by Lawrence Livermore National Laboratory under Contract No. DE-AC52-07NA27344. This document was prepared as an account of work sponsored by an agency of the U.S. government. Neither the U.S. government nor Lawrence Livermore National Security, LLC, nor any of their employees makes any warranty, expressed or implied, or assumes any legal liability or responsibility for the accuracy, completeness, or usefulness of any information, apparatus, product, or process disclosed, or represents that its use would not infringe privately owned rights. Reference herein to any specific commercial product, process, or service by trade name, trademark, manufacturer, or otherwise does not necessarily constitute or imply its endorsement, recommendation, or favoring by the U.S. government or Lawrence Livermore National Security, LLC. The views and opinions of authors expressed herein do not necessarily state or reflect those of the U.S. government or Lawrence Livermore National Security, LLC, and shall not be used for advertising or product endorsement purposes.

APPENDIX

1. Simulation methodology

The simulations were performed using a radiation hydrodynamics plasma physics code HYDRA [31] to model the radiation drive created by the laser-hohlraum interaction and the physics of the capsule implosion. These simulations were performed in a two-step process. First, integrated simulations of the hohlraum and capsule implosion that are benchmarked against experimental data from focused tuning experiments were used to determine the spatially, temporally, and frequency resolved radiation drive surrounding the capsule implosion. Then the radiation drive was extracted and applied to higher-resolution capsule-only total degradation simulations of the implosion to model engineering features with higher fidelity, such as material roughness of the capsule interfaces, a model for the capsule support tent, a model for the DT fill tube [44,45], nonuniformities in ablator thickness, and DT fuel layer thickness together with low-mode nonuniformities of the radiation drive (including modes 1, 2, and 4). The radiation hydrodynamic calculations include detailed equations of state [46,47], radiation particle and neutron transport models [48,49], opacity models [50], and electron-ion coupling [51,52]. In this study, the equation of state model used for the carbon ablator was LEOS table 9067 [53]. The radiation drive was modeled with a flux-limited electron heat transport with a limiter of 0.15, which has been shown to reproduce many radiation drive observables for similar hohlraum conditions [54,55]. An inline cross-beam energy transfer model was used with a saturation clamp on the

electron density fluctuations of the ion acoustic wave ($\delta n/n$). Post-shot simulations (after the experiment) used the measured input target conditions and as-delivered laser powers vs time for all beams which can vary from the requested input conditions.

The simulations were adjusted in a common way between experiments to match tuning data and then applied to simulate the DT layered experiments. These adjustments included artificial multipliers on the input laser power to the integrated simulations to match the in-flight symmetry, in-flight capsule velocity, and shock velocities along two lines of sight (pole and equator). Recent shock timing data prior to N221204 were obtained which improved the symmetry model for temporal variations in the radiation drive when applied to this new design. These data together with the in-flight symmetry and DT hotspot symmetry set the saturation clamp to $\delta n/n = 0.002$ in the foot of the laser pulse until the beginning of the rise to peak power and $\delta n/n = 0.0075$ throughout the remainder of the laser pulse. Backscattered laser light due to interaction of the lasers with the hohlraum wall plasma was energetically low over (210 808, 221 204). This was mostly due to stimulated Brillouin scattering of the inner beams early in peak laser power. The simulations reported here do not model this explicitly, but as part of an effective total laser power multiplier and $\delta n/n$. Recent work suggests that including the measured backscatter time history could impact implosion shape.

For additional details on the simulation methodology see Refs. [9,11,25,56].

2. Additional design details

The design for N221204 used a higher amount of W dopant in the diamond ablator compared to N210808, which, together with the thicker ablator, improved the calculated stability at the accelerating DT-fuel ablator interface. Improving the stability at this interface can increase the amount of clean unmixed DT fuel [57] at large radii near the ablator, which improves its piston efficiency to convert implosion kinetic energy to hotspot internal energy and also results in higher burnup fractions after ignition once the burn wave propagates into the remainder of the DT fuel. For both experiments, the diamond ablators consisted of an inner undoped diamond layer, a W-doped diamond layer at larger radius (0.44 at.% W for N210808 and 0.54–0.6 at.% W for N221204), and an outer undoped diamond layer. The crystal structure was nanocrystalline diamond for both experiments: N210808 (capsule batch KC789) and N221204 (batch KC952). The total ablator thickness was approximately 79 μm for N210808 and approximately 85 μm for N221204. The target quality for KC952 fielded on N221204 was worse than fielded on N210808, with a greater number of high-Z inclusions in the doped ablator layer [12].

As a result of these design changes, the calculated areal density of the diamond ablator and total (fuel plus ablator) and DT fuel at bang time were significantly higher [see Fig. 7 for N221204 (red) compared to N210808 (black)]. Due to the increase in ablator areal density, we estimated a significant improvement in Atwood number for the N221204 design compared to N210808, shown in Fig. 8. The Atwood number

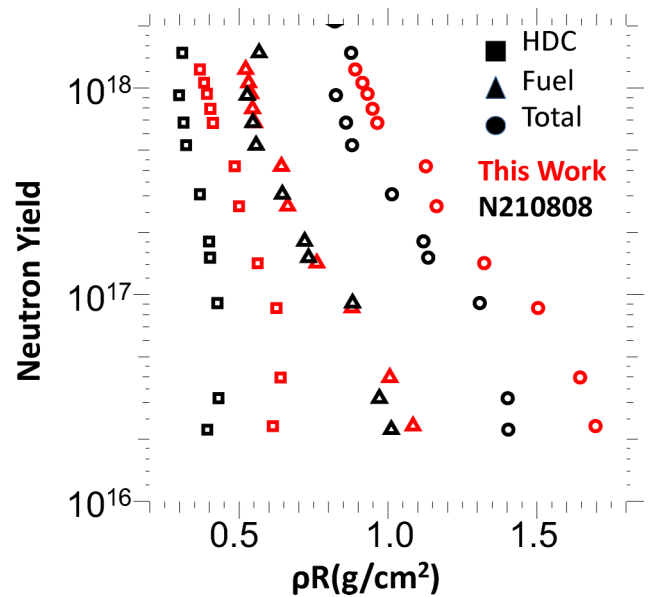


FIG. 7. Calculated neutron yield as a function of areal density (taken at time of peak neutron production) of the HDC diamond ablator (squares), DT fuel (triangles), and total (circles) for the N221204 design (red) compared to N210808 (black) from 1D HYDRA simulations. Here the yield range is sampled by artificially varying the reaction cross sections on these designs. The difference in areal density between the two designs is largest at low yields, with α -particle deposition off, and the areal density for both designs is reduced at higher yields as the burn occurs upon expansion when the hotspot and surrounding dense DT shell are larger.

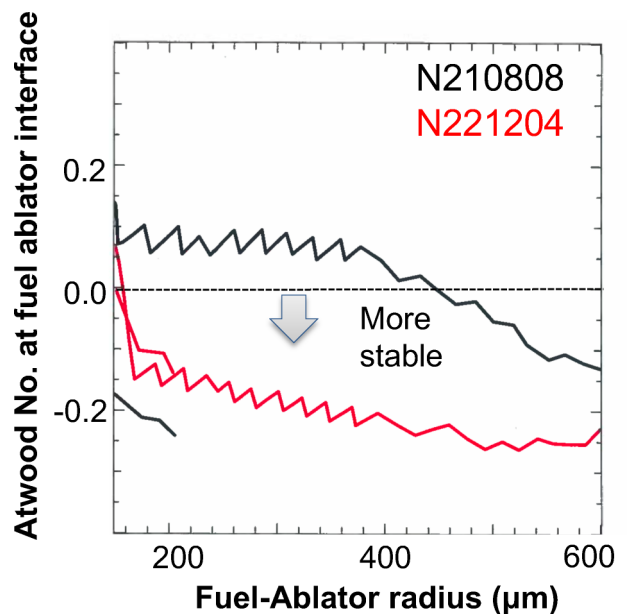


FIG. 8. Calculated Atwood number at the interface between the DT fuel and diamond ablator for N221204 (red curve) compared to N210808 (black curve) as a function of fuel-ablator radius (see the text for details). For an imploding capsule a lower or more negative Atwood number is more stable to Rayleigh-Taylor mixing.

is an important parameter to assess the hydrodynamic stability of a design to Rayleigh-Taylor (RT) instability at material interfaces, defined as $A = (\rho_1 - \rho_2)/(\rho_1 + \rho_2)$, where ρ_1 is the density of the compressed DT fuel and ρ_2 is the density of the remaining ablator material. When this parameter is smaller or negative the accelerating fuel-ablator interface is more stable, reducing growth of the RT instability. In addition, the thicker ablator provides a better in-flight aspect ratio (equal to the ratio of radius to thickness measured at the time of peak acceleration) and a longer distance for perturbations to travel to feed through and impact the implosion.

3. Energy balance

The energy balance of incident laser light into the hohlraum and implosion is estimated using HYDRA 2D simulations calibrated to experimental measurements. We estimate that about 54.1% of the incident laser energy is used to heat the hohlraum wall (of that approximately 4.4% is deposited in the gold lining and approximately 49.7% in the depleted uranium wall), 25.2% of the incident laser energy becomes radiation loss out of the laser entrance holes, 4.5% of the incident laser energy is used to heat the helium gas fill in the hohlraum, and approximately 16.2% is absorbed by the capsule. In addition to these terms, to match experimental data, the laser energy needs to be degraded in simulations by 9%–13%. Then the useful energy coupled to the implosion (and not in the ablated capsule material) is approximately 246 kJ or approximately 12%. The fuel kinetic energy is approximately 15.33 kJ, and the total work done on the DT fuel is approximately 20 kJ (1% of the laser energy). Of this work, approximately 8.2 kJ is coupled to hotspot internal energy.

4. Symmetry optimization

The first attempt to field the new design (N220919) displayed oblate symmetry of approximately $12 \mu\text{m}$ in the primary neutron image, which provides a picture of the hotspot plasma shape. This was in part due to a maximum limit on the wavelength separation, which increases transfer from the outer to inner beams, that could be fielded on the first test due to concerns with laser damage from backscattered laser light via stimulated Brillouin scattering. However, even with this level of hotspot oblateness, the new design resulted in a fusion energy greater than 1 MJ (1.22 MJ, approximately 4.32×10^{17} total neutron yield) due to increased margin for robustness to perturbations, but was significantly lower than the full design potential with good symmetry. Two-dimensional simulations of this experiment (2D total degradation) predicted that improving the symmetry could lead to a greater than $2\times$ increase in fusion energy yield (see Fig. 5).

The simulations with similar hotspot shape but more symmetric dense DT fuel shape give higher yield for a given level of hotspot P2. The asymmetric dense DT fuel shape is caused by fluctuations in the time-dependent radiation drive symmetry. These fluctuations will be directly interrogated via x-ray radiography of the in-flight shell shape earlier in the implosion history, in separate tuning experiments. If the higher-fluctuation cases are experimentally verified, efforts

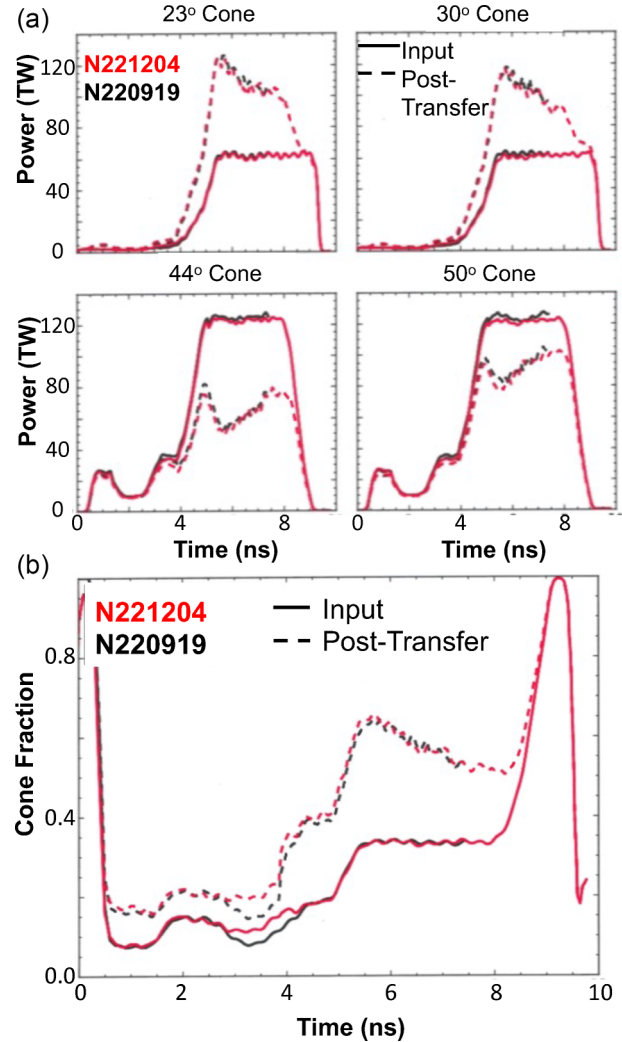


FIG. 9. Changes made to the input laser pulse to reach target gain $G > 1$ following the first new design attempt N220919 (1.22 MJ) and N221204 (3.15 MJ). (a) The amount of transfer was increased for N221204 (red) compared to N220919 (black) via increasing $\Delta\lambda$ from 2.5 \AA to 2.75 \AA . The input laser powers (solid lines) and calculated laser powers (dashed lines) are shown for all cones post energy transfer for N221204 (red) vs N220919 (black). (bottom) The requested input cone fractions (solid lines) were also adjusted, i.e., the ratio of the inner cone power to total laser power, to optimize the time-dependent symmetry based on the updated hohlraum model (see Sec. 1 of the Appendix). The post-transfer cone fractions (dashed lines) are shown for N221204 (red) vs N220919 (black).

to further optimize implosion symmetry will continue and should significantly improve the yield. If the lower-fluctuation (higher-yield) cases are experimentally verified, the difference in yield between the simulations and N221204 could be attributed to known diamond capsule defects present in these experiments [12], which will also be tested in future experiments fielding higher-quality diamond capsules.

The hotspot symmetry improvement was the only change between N220919 ($P2 = -12 \mu\text{m}$) and N210808 ($P2 = \sim 0 \mu\text{m}$) accomplished by adjusting the laser input conditions to achieve a symmetric radiation drive surrounding the capsule early in the pulse and swinging the inner drive a little

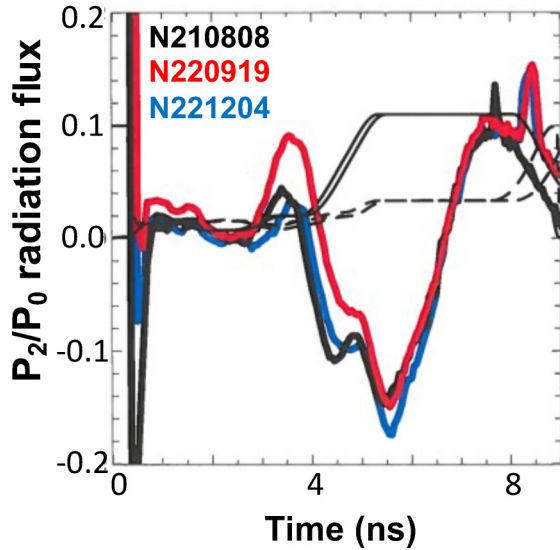


FIG. 10. Mode 2 of the simulated Legendre decomposition of the radiation flux asymmetry (P_2/P_0) for N210808 (black) N220910 (red) and N221204 (blue) plotted together with the scaled requested laser power as a function of time (black solid lines), and cone fraction (ratio of inner laser cones to total power) as a function of time (dashed lines). The P_2 decomposition is within the specification during the foot, until the rise to peak power, but is allowed to swing during the peak of the pulse (see the text for details). Values of $P_2/P_0 < 0$ have higher radiation temperature at the waist of the hohlraum.

higher to account for the later-time reduction in inner waist drive as the hohlraum plasma fills. To increase drive at the waist of the hohlraum during the peak of the pulse, the amount of laser power transferred from the outer to inner beams (CBET) was increased by increasing the wavelength detuning [$\Delta\lambda = (\text{inner beam}) - (\text{outer beam})$ before laser frequency tripling] [23–26] from $\Delta\lambda = 2.5 \text{ \AA}$ for N210919 to $\Delta\lambda = 2.75 \text{ \AA}$ for N221204. Since late-time laser beam propagation through the plasma filled hohlraum is difficult to model, a data-driven model [30] was used together with an experimental sensitivity curve hotspot P_2 vs $\Delta\lambda$ to set the optimal wavelength separation for N221204 (see also [9]). We also used simulations to predict changes in symmetry from prior experiments, such as the impact of the extra diamond ablator payload on symmetry. The additional transfer can be seen in Fig. 9(a), which shows the pre- and post-CBET transfer powers on all four laser cones (inner 23° and 23° and outer 44° and 50° cones). Figure 9(b) shows the pre- and post-CBET cone fraction (ratio of power on the inner cone to total power) for N221204 vs N210808.

The intentional increase in energy transfer during the peak of the pulse also resulted in more transfer during the foot of the pulse (before the rise to peak power), which was then reoptimized by adjusting the time-dependent foot cone fraction [11,25,55] (ratio of power on the inner cone to total power) [see Fig. 9(b)]. Typically, as the transfer is turned up in the peak, the optimal early-time cone fraction (before 4.5 ns) is turned down to account for the additional transfer in achieving optimal time-dependent symmetry. However, here the cone fraction was increased for N221204 compared to N220919 even with a large amount of CBET to respond to shock symmetry data taken directly before this experiment (N221106), which showed a smaller asymmetry in the foot at lower wavelength separations for prior tuning experiments. The hohlraum model was adjusted to these data by modifying the CBET saturation and gave a better extrapolation for foot symmetry tuning at higher wavelength separation. This new model was verified in a shock timing experiment (N230110) following N221204 which enabled tuning a symmetric foot leading to lower asymmetries in the compressed fuel ρR .

Cross-beam energy transfer is used to control the symmetry instead of varying the peak laser power between the cones, to enable using maximum energy of the NIF laser. Controlling the symmetry by varying laser power alone would require reducing the outer beam power to 150–200 TW from a maximum 440 TW at 2.05 MJ, forgoing the benefit of increased laser energy.

Given these changes in wavelength detuning and input cone fractions, the resulting post-transfer change to the mode 2 Legendre moment of the radiation flux asymmetry is shown in Fig. 10 for N220919 vs N221204, compared to N210808. Also shown are the scaled laser pulses and cone fractions as a function of time. Since the outer beams are “drooping,” or ramping down, late in time while the inner beams are being held on, this causes the late-time increase in cone fraction. This drooping was incorporated into the design to enable using the full NIF energy and power on all 192 laser beams, increase the late-time ablation pressure, and mitigate potential laser backscattering out of the hohlraum late in time from the outer beams which interact with the high- Z expanding wall plasma. The cone fraction in the peak (33%) was also chosen (together with the shape of the droop) to enable the full use of NIF at maximum power. This results in a swing in the temporal P_2 flux asymmetry during the peak of the pulse, which transitions from being higher temperature at the waist to higher temperature at the poles as the wall enters and blocks the inner beams from reaching the center of the hohlraum. If this swing can be balanced, the imploding shell and hotspot symmetry can be maintained.

- [1] E. I. Moses, J. Atherton, L. Lagin, D. Larson, C. Keane, B. MacGowan, R. Patterson, M. Spaeth, B. Van Wousterghem, P. Wegner, and R. Kauffman, The National Ignition Facility: Transition to a user facility, *J. Phys.: Conf. Ser.* **688**, 012073 (2016).
- [2] S. E. Koonin, G. F. Carrier, R. Christy, R. Conn, R. Davidson, J. Dawson, A. DeMaria, P. Doty, W. Happer, Jr., G. L. Kulcinski *et al.*, Review of the department of energy’s inertial confinement fusion program, *J. Fusion Energy* **10**, 157 (1991).

- [3] J. Nuckolls, L. Wood, A. Thiessen, and G. Zimmerman, Laser compression of matter to super-high densities: Thermonuclear (CTR) applications, *Nature (London)* **239**, 139 (1972).
- [4] J. S. Clarke, H. N. Fisher, and R. J. Mason, Laser-driven implosion of spherical DT targets to thermonuclear burn conditions, *Phys. Rev. Lett.* **30**, 249 (1973).

- [5] R. F. Post, Controlled fusion research—An application of the physics of high temperature plasmas, *Rev. Mod. Phys.* **28**, 338 (1956).
- [6] G. S. Fraley, E. J. Linnebur, R. J. Mason, and R. L. Morse, Thermonuclear burn characteristics of compressed deuterium-tritium microsphere, *Phys. Fluids* **17**, 474 (1974).
- [7] J. D. Lawson, Some criteria for a power producing thermonuclear reactor, *Proc. Phys. Soc. B* **70**, 6 (1957).
- [8] H. Abu-Shawareb *et al.* (Indirect Drive ICF Collaboration), Lawson's criterion for ignition achieved in an inertial fusion experiment, *Phys. Rev. Lett.* **129**, 075001 (2022).
- [9] A. L. Kritcher, A. B. Zylstra, D. A. Callahan, O. A. Hurricane, C. R. Weber, D. S. Clark, C. V. Young, J. E. Ralph, D. T. Casey, A. Pak, O. L. Landen *et al.*, Design of an inertial fusion experiment exceeding the Lawson criterion for ignition, *Phys. Rev. E* **106**, 025201 (2022).
- [10] A. B. Zylstra, A. L. Kritcher, O. A. Hurricane, D. A. Callahan, J. E. Ralph, D. T. Casey, A. Pak, O. L. Landen, B. Bachmann, K. Baker *et al.*, Experimental achievement and signatures of ignition at the National Ignition Facility, *Phys. Rev. E* **106**, 025202 (2022).
- [11] A. L. Kritcher, C. V. Young, H. F. Robey, C. R. Weber, A. B. Zylstra, O. A. Hurricane, D. A. Callahan, J. E. Ralph, J. S. Ross, K. L. Baker *et al.*, Design of inertial fusion implosions reaching the burning plasma regime, *Nat. Phys.* **18**, 251 (2022).
- [12] A. Pak, A. B. Zylstra, K. L. Baker, D. T. Casey, E. Dewald, L. Divol, M. Hohenberger, A. S. Moore, J. E. Ralph, D. J. Schlossberg *et al.*, preceding paper, Observations and properties of the first laboratory fusion experiment to exceed a target gain of unity, *Phys. Rev. E* **109**, 025203 (2024).
- [13] O. A. Hurricane, D. A. Callahan, D. T. Casey, A. R. Christopherson, A. L. Kritcher, O. L. Landen, S. A. MacLaren, R. Nora, P. K. Patel, J. Ralph, D. Schlossberg, P. T. Springer, C. V. Young, and A. B. Zylstra, Energy principles of scientific breakeven in an inertial fusion experiment, *Phys. Rev. Lett.* **132**, 065103 (2024).
- [14] H. Abu-Shawareb *et al.* (The Indirect Drive ICF Collaboration), Achievement of target gain larger than unity in an inertial fusion experiment, *Phys. Rev. Lett.* **132**, 065102 (2024).
- [15] J.-M. G. Di Nicola, T. Suratwala, L. Pelz, J. Heebner, D. Alessi, A. Bhasker, T. Bond, M. Bowers, G. Brunton, B. Buckley *et al.*, in *Proceedings of the International Conference on High Power Lasers for Fusion Research VII*, edited by A. A. S. Awwal and C. L. Haefner, SPIE Proc. Vol. PC12401 (SPIE, Bellingham, 2023), p. PC124013.
- [16] J. D. Nicola, T. Bond, M. Bowers, L. Chang, M. Hermann, R. House, T. Lewis, K. Manes, G. Mennerat, B. MacGowan, R. Negres, B. Olejniczak, C. Orth, T. Parham, S. Rana, B. Raymond, M. Rever, S. Schrauth, M. Shaw, M. Spaeth *et al.*, The National Ignition Facility: Laser performance status and performance quad results at elevated energy, *Nucl. Fusion* **59**, 032004 (2019).
- [17] M. S. Rubery, M. D. Rosen, N. Aybar, O. L. Landen, L. Divol, C. V. Young, C. Weber, J. Hammer, J. D. Moody, A. S. Moore, A. L. Kritcher, A. B. Zylstra, O. Hurricane, A. E. Pak, S. MacLaren, G. Zimmerman, J. Harte, and T. Woods, Hohlräum reheating from burning NIF implosions, *Phys. Rev. Lett.* **132**, 065104 (2024).
- [18] J. Lindl, Development of the indirect-drive approach to inertial confinement fusion and the target physics basis for ignition and gain, *Phys. Plasmas* **2**, 3933 (1995).
- [19] J. D. Lindl, P. Amendt, R. L. Berger, S. G. Glendinning, S. H. Glenzer, S. W. Haan, R. L. Kauffman, O. L. Landen, and L. J. Suter, The physics basis for ignition using indirect-drive targets on the National Ignition Facility, *Phys. Plasmas* **11**, 339 (2004).
- [20] S. W. Haan, J. D. Lindl, D. A. Callahan, D. S. Clark, J. D. Salmonson, B. A. Hammel, L. J. Atherton, R. C. Cook, M. J. Edwards, S. H. Glenzer *et al.*, Point design targets, specifications, and requirements for the 2010 ignition campaign on the National Ignition Facility, *Phys. Plasmas* **18**, 051001 (2011).
- [21] O. A. Hurricane, A. Kritcher, D. A. Callahan, O. Landen, P. K. Patel, P. T. Springer, D. T. Casey, E. L. Dewald, T. R. Dittrich, T. Döppner *et al.*, On the importance of minimizing “coast-time” in x-ray driven inertially confined fusion implosions, *Phys. Plasmas* **24**, 092706 (2017).
- [22] A. L. Kritcher, R. Town, D. Bradley, D. Clark, B. Spears, O. Jones, S. Haan, P. T. Springer, J. Lindl, R. H. H. Scott *et al.*, Metrics for long wavelength asymmetries in inertial confinement fusion implosions on the National Ignition Facility, *Phys. Plasmas* **21**, 042708 (2014).
- [23] P. Michel, L. Divol, E. A. Williams, S. Weber, C. A. Thomas, D. A. Callahan, S. W. Haan, J. D. Salmonson, S. Dixit, D. E. Hinkel *et al.*, Tuning the implosion symmetry of ICF targets via controlled crossed-beam energy transfer, *Phys. Rev. Lett.* **102**, 025004 (2009).
- [24] J. D. Moody, P. Michel, L. Divol, R. L. Berger, E. Bond, D. K. Bradley, D. A. Callahan, E. L. Dewald, S. Dixit, M. J. Edwards *et al.*, Multistep redirection by cross-beam power transfer of ultrahigh-power lasers in a plasma, *Nat. Phys.* **8**, 344 (2012).
- [25] A. L. Kritcher, J. Ralph, D. E. Hinkel, T. Döppner, M. Millot, D. Mariscal, R. Benedetti, D. J. Strozzi, T. Chapman, C. Goyon *et al.*, Energy transfer between lasers in low-gas-fill-density hohlraums, *Phys. Rev. E* **98**, 053206 (2018).
- [26] L. A. Pickworth, T. Doepfner, D. E. Hinkel, J. E. Ralph, B. Bachmann, L. P. Masse, L. Divol, L. R. Benedetti, P. M. Celliers, H. Chen *et al.*, Application of cross-beam energy transfer to control drive symmetry in ICF implosions in low gas fill *Hohlraums* at the National Ignition Facility, *Phys. Plasmas* **27**, 102702 (2020).
- [27] S. L. Pape, L. F. Berzak Hopkins, L. Divol, N. Meezan, D. Turnbull, A. J. Mackinnon, D. Ho, J. S. Ross, S. Khan, A. Pak *et al.*, The near vacuum hohlraum campaign at the NIF: A new approach, *Phys. Plasmas* **23**, 056311 (2016).
- [28] L. F. Berzak Hopkins, N. B. Meezan, S. Le Pape, L. Divol, A. J. Mackinnon, D. D. Ho, M. Hohenberger, O. S. Jones, G. Kyrala, J. L. Milovich *et al.*, First high-convergence cryogenic implosion in a near-vacuum hohlraum, *Phys. Rev. Lett.* **114**, 175001 (2015).
- [29] L. Divol, A. Pak, L. F. B. Hopkins, S. L. Pape, N. B. Meezan, E. L. Dewald, D. D.-M. Ho, S. F. Khan, A. J. Mackinnon, J. S. Ross *et al.*, Symmetry control of an indirectly driven high-density-carbon implosion at high convergence and high velocity, *Phys. Plasmas* **24**, 056309 (2017).
- [30] D. A. Callahan, O. A. Hurricane, J. E. Ralph, C. A. Thomas, K. L. Baker, L. R. Benedetti, L. F. Berzak Hopkins, D. T. Casey, T. Chapman, C. E. Czajka *et al.*, Exploring the limits of case-to-capsule ratio, pulse length, and picket energy for symmetric hohlraum drive on the National Ignition Facility Laser, *Phys. Plasmas* **25**, 056305 (2018).
- [31] M. M. Marinak, G. D. Kerbel, N. A. Gentile, O. Jones, D. Munro, S. Pollaine, T. R. Dittrich, and S. W. Haan, Three-

- dimensional HYDRA simulations of National Ignition Facility targets, *Phys. Plasmas* **8**, 2275 (2001).
- [32] D. J. Strozzi, D. S. Bailey, P. Michel, L. Divol, S. M. Sepke, G. D. Kerbel, C. A. Thomas, J. E. Ralph, J. D. Moody, and M. B. Schneider, Interplay of laser-plasma interactions and inertial fusion hydrodynamics, *Phys. Rev. Lett.* **118**, 025002 (2017).
- [33] J. D. Lindl, S. W. Haan, O. L. Landen, A. R. Christopherson, and R. Betti, Progress toward a self-consistent set of 1D ignition capsule metrics in ICF, *Phys. Plasmas* **25**, 122704 (2018).
- [34] D. Casey, B. MacGowan, O. Hurricane, O. Landen, R. Nora, S. Haan, A. Kritcher, A. Zylstra, J. Ralph, E. Dewald *et al.*, Diagnosing the origin and impact of low-mode asymmetries in ignition experiments at the National Ignition Facility, *Phys. Rev. E* **108**, L053203 (2023).
- [35] O. A. Hurricane, D. T. Casey, O. Landen, A. L. Kritcher, R. Nora, P. K. Patel, J. A. Gaffney, K. D. Humbird, J. E. Field, M. K. G. Kruse, J. L. Peterson, and B. K. Spears, An analytic asymmetric-piston model for the impact of mode-1 shell asymmetry on ICF implosions, *Phys. Plasmas* **27**, 062704 (2020).
- [36] B. MacGowan, O. Landen, D. Casey, C. Young, D. Callahan, E. Hartouni, R. Hatarik, M. Hohenberger, T. Ma, D. Mariscal *et al.*, Trending low mode asymmetries in NIF capsule drive using a simple viewfactor metric, *High Energy Density Phys.* **40**, 100944 (2021).
- [37] D. T. Casey, B. J. MacGowan, J. D. Sater, A. B. Zylstra, O. L. Landen, J. Milovich, O. A. Hurricane, A. L. Kritcher, M. Hohenberger, K. Baker *et al.*, Evidence of three-dimensional asymmetries seeded by high-density carbon-ablator nonuniformity in experiments at the National Ignition Facility, *Phys. Rev. Lett.* **126**, 025002 (2021).
- [38] A. Pak, L. Divol, C. R. Weber, L. F. B. Hopkins, D. S. Clark, E. L. Dewald, D. N. Fittinghoff, V. Geppert-Kleinrath, M. Hohenberger, S. Le Pape *et al.*, Impact of localized radiative loss on inertial confinement fusion implosions, *Phys. Rev. Lett.* **124**, 145001 (2020).
- [39] O. A. Hurricane, D. T. Casey, O. Landen, D. A. Callahan, R. Bionta, S. Haan, A. L. Kritcher, R. Nora, P. K. Patel, P. T. Springer, and A. Zylstra, Extensions of a classical mechanics “piston-model” for understanding the impact of asymmetry on ICF implosions: The cases of mode 2, mode 2/1 coupling, time-dependent asymmetry, and the relationship to coast-time, *Phys. Plasmas* **29**, 012703 (2022).
- [40] P. K. Patel, P. T. Springer, C. R. Weber, L. C. Jarrott, O. A. Hurricane, B. Bachmann, K. L. Baker, L. F. B. Hopkins, D. A. Callahan, D. Casey *et al.*, Hotspot conditions achieved in inertial confinement fusion experiments on the National Ignition Facility, *Phys. Plasmas* **27**, 050901 (2020).
- [41] J. Lindl, S. Haan, and O. L. Landen, Impact of hohlraum cooling on ignition metrics for inertial fusion implosions, *Phys. Plasmas* **30**, 012705 (2023).
- [42] O. A. Hurricane, D. A. Callahan, P. T. Springer, M. J. Edwards, P. Patel, K. Baker, D. T. Casey, L. Divol, T. Doepfner, D. E. Hinkel *et al.*, Beyond alpha-heating: Driving inertially confined fusion implosions toward a burning-plasma state on the National Ignition Facility, *Plasma Phys. Control. Fusion* **61**, 014033 (2019).
- [43] B. K. Spears, S. Brandon, J. E. Field, J. Gaffney, K. D. Humbird, K. A. L., M. K. G. Kruse, E. Kur, B. Kustowski, D. Munro *et al.*, A physics-informed machine learning model quantitatively predicted fusion ignition at the national ignition facility (unpublished).
- [44] D. S. Clark, C. R. Weber, J. L. Milovich, J. D. Salmonson, A. L. Kritcher, S. W. Haan, B. A. Hammel, D. E. Hinkel, O. A. Hurricane, O. S. Jones *et al.*, Three-dimensional simulations of low foot and high foot implosion experiments on the National Ignition Facility, *Phys. Plasmas* **23**, 056302 (2016).
- [45] D. S. Clark, C. R. Weber, J. L. Milovich, A. E. Pak, D. T. Casey, B. A. Hammel, D. D. Ho, O. S. Jones, J. M. Koning, A. L. Kritcher *et al.*, Three-dimensional modeling and hydrodynamic scaling of National Ignition Facility implosions, *Phys. Plasmas* **26**, 050601 (2019).
- [46] L. X. Benedict, K. P. Driver, S. Hamel, B. Militzer, T. Qi, A. A. Correa, A. Saul, and E. Schwegler, Multiphase equation of state for carbon addressing high pressures and temperatures, *Phys. Rev. B* **89**, 224109 (2014).
- [47] J. Gaffney, S. Hu, P. Arnault, A. Becker, L. Benedict, T. Boehly, P. Celliers, D. Ceperley, O. Certik, J. Clerouin *et al.*, A review of equation-of-state models for inertial confinement fusion materials, *High Energy Density Phys.* **28**, 7 (2018).
- [48] M. P. Desjarlais, C. R. Scullard, L. X. Benedict, H. D. Whitley, and R. Redmer, Density-functional calculations of transport properties in the nondegenerate limit and the role of electron-electron scattering, *Phys. Rev. E* **95**, 033203 (2017).
- [49] L. G. Stanton and M. S. Murillo, Ionic transport in high-energy-density matter, *Phys. Rev. E* **93**, 043203 (2016).
- [50] C. A. Iglesias and F. J. Rogers, Updated opal opacities, *Astrophys. J.* **464**, 943 (1996).
- [51] Y. Lee and R. More, An electron conductivity model for dense plasmas, *Phys. Fluids* **27**, 1273 (1984).
- [52] C. R. Scullard, S. Serna, L. X. Benedict, C. L. Ellison, and F. R. Graziani, Analytic expressions for electron-ion temperature equilibration rates from the Lenard-Balescu equation, *Phys. Rev. E* **97**, 013205 (2018).
- [53] A. A. Correa, L. X. Benedict, D. A. Young, E. Schwegler, and S. A. Bonev, First-principles multiphase equation of state of carbon under extreme conditions, *Phys. Rev. B* **78**, 024101 (2008).
- [54] W. A. Farmer, C. Ruyer, J. A. Harte, D. E. Hinkel, D. S. Bailey, E. Kur, O. L. Landen, N. Lemos, P. A. Michel, D. J. Strozzi, C. R. Weber, and G. B. Zimmerman, Impact of flow-induced beam deflection on beam propagation in ignition scale hohlraums, *Phys. Plasmas* (to be published).
- [55] A. L. Kritcher, A. B. Zylstra, D. A. Callahan, O. A. Hurricane, C. Weber, J. Ralph, D. T. Casey, A. Pak, K. Baker, B. Bachmann *et al.*, Achieving record hot spot energies with large HDC implosions on NIF in Hybrid-E, *Phys. Plasmas* **28**, 072706 (2021).
- [56] A. L. Kritcher, D. T. Casey, C. A. Thomas, A. Zylstra, M. Hohenberger, K. Baker, S. Le Pape, B. Bachmann, S. Bhandarkar, J. Biener *et al.*, Symmetric fielding of the largest diamond capsule implosions on the NIF, *Phys. Plasmas* **27**, 052710 (2020).
- [57] B. Bachmann, S. A. MacLaren, L. Masse, S. Bhandarkar, T. Briggs, D. Casey, L. Divol, T. Doepfner, D. Fittinghoff, M. Freeman, S. Haan, G. N. Hall, B. Hammel, E. Hartouni, N. Izumi, V. Geppert-Kleinrath, S. Khan, B. Kozioziemski, C. Krauland, O. Landen *et al.*, Measuring and simulating ice-ablator mix in inertial confinement fusion, *Phys. Plasmas* **30**, 052704 (2023).